Journal of Materials Chemistry C

ROYAL SOCIETY OF CHEMISTRY

PAPER

View Article Online
View Journal | View Issue

Cite this: *J. Mater. Chem. C*, 2025, **13**, 22625

Ubiquitous shallow trap states and lattice hydrogenation of ZnO particles

Korbinian Aicher, Thomas Berger, Ulrich Aschauer * and Oliver Diwald *

ZnO nanoparticle powders are an important and common starting material for functional devices that require the highest purity for electronic and optical applications. In this combined experimental and *ab initio* study, we use electron paramagnetic resonance (EPR) spectroscopy to detect shallow donor states in the ZnO lattice *via* their characteristic paramagnetic resonance at g = 1.96. Using DFT calculations that account for the chemical environment and the high temperatures during the gas-phase synthesis in conjunction with control experiments with atomic hydrogen, we demonstrate that these paramagnetic defects correspond to neutral hydrogenated oxygen sites (OH_O^0). As a key implication of these findings, ZnO particle powders, although produced under the pure conditions of gas-phase synthesis and subsequently annealed in a vacuum to 873 K, were found to be doped with hydrogen at a base concentration of $c > 10^{-5}$ at%. This, in turn, highlights the overlooked role of unwanted hydrogen in nanoscale ZnO as components for applications in optics, electronics, and sensing.

Received 11th August 2025,
Accepted 1st October 2025

DOI: 10.1039/d5tc03036f

rsc.li/materials-c

1. Introduction

Zinc oxide (ZnO) nanostructures are of great interest because of their functional properties that find application in a wide range of processes and devices, including varistors,[1–3] sensors,[4–8] thin-film transistors,[9] (photo)catalysts,[3,10–13] and (photo)electrodes.[14,15] Moreover, ZnO is a prototype material for defect chemistry studies. Indeed, it was shown that processing ZnO particles and nanoparticles to manufacture ceramics (*e.g.*, for varistors, sensors, *etc.*) and related particle-based materials, such as electrodes or catalysts, can substantially influence the concentration of (functional) point defects inside the lattice.

Recent investigations have shown that cold sinter processing (CSP) of ZnO, *i.e.*, material compaction and densification at temperatures of 200 °C and below, leads to the depletion of lattice oxygen. A continuous increase of near infrared (NIR) absorption at wavelengths above 1000 nm was measured with diffuse reflectance (DR) spectroscopy, whereas electron paramagnetic resonance (EPR) revealed significantly increased spin concentrations that are related to the formation of paramagnetic defects resonating at g = 1.96. The fact that CSP treatment was performed with aqueous acetic acid solution as a transient phase has prompted mechanistic questions and led to the hypothesis that the underlying paramagnetic shallow trap states correspond to protonated sites of the anionic sublattice.[16]

The facilitated uptake of process-related impurities in highly dispersed solids due to their high specific surface area has been largely overlooked in the past, although it could be associated with the emergence of point defects with desired or undesired doping effects or functional properties.[17] Regarding the challenge of materials synthesis-related impurity effects, gas-phase synthesis is considered a relatively clean method compared to liquid-phase synthesis.[18] The starting materials are metals, metal–organic precursors (*i.e.*, compounds exclusively composed of carbon, hydrogen, and oxygen, apart from the metal) that transform at high temperatures into solid nuclei which further grow to nanoparticles and particles.[18] (As a substantial difference between nanocrystals that are grown in the liquid phase, drying of nanoparticle ensembles is associated with the conversion of solid–liquid interfaces into solid–gas and solid–solid interfaces. Whenever solvents and surface grafted molecules are involved, their removal by vacuum treatment at elevated temperatures inevitably increases the probability of impurity incorporation and particle aggregation. The latter process corresponds to solid–solid interface formation.)

Electron paramagnetic resonance (EPR) studies of ZnO materials that were grown using very different synthesis approaches commonly reveal paramagnetic resonances at g = 1.96. Despite the high number of reports, the microscopic origin of this apparently ubiquitous EPR signal has remained a subject of debate in the literature, with various intrinsic and extrinsic defect mechanisms proposed.[19–24] Since this study focuses on intrinsic defects and hydrogen as the only extrinsic impurity, we only briefly refer the reader to comprehensive reviews by Ischenko *et al.*,[25] Djurišić *et al.*,[26] and Stehr *et al.*[27] In contrast,

Department of Chemistry and Physics of Materials, Paris-Lodron University Salzburg, Jakob-Haringer-Straße 2a, A-5020 Salzburg, Austria.
E-mail: oliver.diwald@plus.ac.at, ulrichjohannes.aschauer@plus.ac.at

the present work focuses exclusively on the defect centers observed in our gas-phase synthesized ZnO nanoparticles.

For this work, two types of ZnO nanoparticle powders, synthesized either *via* chemical vapor synthesis (CVS) or flame spray pyrolysis (FSP), were compared to determine the influence of the synthesis method on defect formation. This approach was motivated by findings on TiO_2 from Elser *et al.*,[28] demonstrating that TiO_2 nanoparticles produced by FSP exhibited a high prevalence of coalescing into dimers and trimers with a significant number of interparticle necks where surface carbon impurities become entrapped and transform into substitutional point defects. In contrast, CVS-synthesized TiO_2 nanoparticles formed only agglomerates without evidence of necking or partial particle fusion. This distinct aggregation behavior suggests that, even for gas-phase synthesis, the production method affects the resulting powders' microstructures and ultimately determines the defect population of ZnO nanoparticles at different stages of materials processing.

The present investigation combines experimental and theoretical methods and addresses the origin of the $g = 1.96$ signal. EPR spectroscopy is employed to analyze ZnO nanoparticle powders obtained *via* gas-phase synthesis, processed at elevated temperatures in an oxygen atmosphere and characterized under – in terms of pressure and composition of the environmental gas phase – well controlled conditions. In parallel, density functional theory (DFT) calculations were used to predict the charge state and concentration of defects potentially responsible for the observed paramagnetic signature. This integrated approach identifies ZnO lattice hydrogenation as the most probable source for the widely reported EPR signal at $g = 1.96$. The resulting understanding of defect-related spin signatures in ZnO underlines the important and subtle relationship between chemical materials synthesis and functional defects in the final material.

2. Experimental section

2.1. Nanoparticle synthesis & thermal annealing

ZnO nanoparticles were produced *via* chemical vapor synthesis (CVS) and flame spray pyrolysis (FSP).

Chemical vapor synthesis (CVS). For the synthesis of ZnO nanoparticles *via* metal–organic chemical vapor synthesis (MO-CVS), zinc acetate dihydrate (Sigma-Aldrich, ≥99.0%) was subjected to combustion in a flow reactor in O_2 atmosphere ($p(O_2) = 15$ mbar, flowrate: 650 sccm). Further details about the synthesis conditions can be found in ref. 29.

Flame spray pyrolysis (FSP). Details about the self-constructed flame spray apparatus and the synthesis conditions can be found in ref. 30 and 31.

To prepare the precursor solution, 16.46 g zinc acetate dihydrate (Sigma-Aldrich, ≥99.0%) were dissolved in a solvent mixture comprising 20 mL of methanol (≥99.8%, Sigma Aldrich), 33.4 mL of 2-ethylhexanoic acid (≥99%, Sigma Aldrich) and 39 mL of xylene (≥98.5%, VWR Chemicals), yielding a zinc concentration of $c_{Zn} = 0.75$ mol L^{-1}. The mixture was refluxed for 3 hours at 323 K using a reflux condenser.

Thermal annealing. The thermal annealing programs consist of three steps, which are schematically illustrated in the SI (Fig. S1).

In the first step, the ZnO nanoparticle powder is heated up to 473 K at the rate of 2.5 K min^{-1} under continuous pumping at a dynamic high vacuum of $p < 10^{-5}$ mbar and dwelled for 30 minutes. Afterwards, the sample is cooled down to room temperature. In the second step, 650 mbar of molecular oxygen (O_2 5.0) is added, and the sample is heated either to 573 K or to 673 K (depending on the annealing program) using a rate of 5 K min^{-1}. After a dwell time of 30 minutes, the sample is cooled to room temperature and subsequently re-evacuated to high vacuum ($p < 10^{-5}$ mbar). In the third and final step, 650 mbar of molecular oxygen (O_2 5.0) are added, and the sample is heated either to 673 K or to 873 K (depending on the annealing program) using a rate of 5 K min^{-1} and a dwell time of 60 minutes. The sample is then cooled to room temperature and re-evacuated to high vacuum ($p < 10^{-5}$ mbar). Samples annealed to final temperatures of 673 K and 873 K are referred to as VA673 and VA873, respectively.

2.2. Hydrogen exposure experiments

For sample exposure to atomic and molecular hydrogen, a continuous flow of molecular hydrogen was adjusted within a dedicated high vacuum system to yield a constant background pressure of $p(H_2) = 7 \times 10^{-3}$ mbar. This system enables sample treatment under well-defined gas atmospheres – including high vacuum conditions ($p < 10^{-5}$ mbar), atomic and molecular hydrogen, and molecular oxygen – over a temperature range from room temperature up to 873 K.[32] A coiled tungsten filament heated to approximately 2000 K was used to produce atomic hydrogen *via* the homolytic dissociation of molecular hydrogen. The ZnO nanoparticle powders were exposed to either atomic or molecular hydrogen at room temperature for three hours within dedicated vacuum-tight silica cells, comprising a quartz glass chamber capable of withstanding thermal annealing up to 1173 K and a Suprasil quartz glass tube used for EPR measurements.

2.3. Materials characterization

Transmission electron microscopy. Transmission electron microscopy (TEM) data were acquired using a JEOL JEM-F200 transmission electron microscope operated at 200 kV equipped with a cold field-emission electron source. TEM images to access morphological and structural information were recorded using a TVIPS F216 2k by 2k CMOS camera. Evaluation of images acquired during TEM analysis was performed with the EM Measure software from TVIPS.

Electron paramagnetic resonance. Continuous wave (CW) electron paramagnetic resonance (EPR) measurements were conducted using a Bruker EMX plus-10/12/P/L X-band spectrometer, equipped with an EMX^{Plus} standard cavity. The resonant magnetic field values were accurately determined using an NMR teslameter. A Suprasil quartz glass tube ($d_o = 5$ mm, $d_i = 3$ mm) containing ZnO nanoparticle powders was connected to a high vacuum line with base pressures as low as

$p < 10^{-5}$ mbar. This setup allows the addition of pure gases (O_2) and annealing in controlled atmospheres, including high vacuum conditions ($p < 10^{-5}$ mbar). EPR spectra were recorded either at 100 K under continuous pumping for high vacuum conditions ($p < 10^{-5}$ mbar), in pure oxygen gas ($p(O_2)$ = 100 mbar) using a variable temperature unit (Bruker), or at 10 K under static vacuum conditions ($p \approx 10^{-4}$ mbar) using a waveguide cryogen-free system (Oxford Instruments). Typical acquisition parameters are a microwave power of 1 mW, a field modulation frequency of 100 kHz, and a modulation amplitude of 0.2 mT.

To quantify the spins, the procedure for calculating the number of spins in the Bruker Xenon software was utilized. This method allows the direct determination of the number of unpaired spins in the sample without the need for a reference standard. The underlying formulation is shown in eqn (1).

$$N_S = \frac{DI \cdot V}{P \cdot B_m \cdot Q \cdot c \cdot S \cdot (S+1) \cdot n_B \cdot f(B_1, B_m)} \quad (1)$$

The acquisition parameters – microwave power P, modulation amplitude B_m, and resonator Q-factor Q – are specific to each measurement and automatically stored by the software. Resonator properties, including the calibration factor c and field profile $f(B_1,B_m)$, are also accounted for in the software and have been determined during factory calibration using a known standard. The Boltzmann factor n_B is computed based on the sample temperature and microwave frequency, both of which depend on the measurement and are recorded by the software. The double integral DI is determined through a two-step integration of the analyzed EPR signal. Electron spin S, sample position within the resonator, and sample volume V must be manually input by the user in the software's processing dialog. The sample volume V is determined by the inner diameter of the EPR tube and the sample length.

Microwave power saturation curves were recorded to investigate saturation behavior. Therefore, the microwave attenuation gain was varied from 0 to 50 dB in 5 dB increments, corresponding to microwave power values ranging from 200 mW to 0.002 mW.

2.4. Density functional theory calculations

Spin-polarized density functional theory (DFT) calculations were performed using the planewave-pseudopotential formalism as implemented in the VASP code.[33–35] Since the band gap of ZnO is severely underestimated using semi-local density functionals, we followed a two-step procedure to properly capture gap states. In the first step, internal coordinates (and for the stoichiometric case also the cell) were relaxed using the PBE functional.[36] Afterwards, we performed a single SCF calculation using the HSE06 hybrid functional[37] starting from the PBE wavefunctions. For PBE calculations, wavefunctions were expanded in planewaves up to a kinetic energy cutoff of 520 eV, which, to ease the computational burden, had to be reduced to 400 eV for the HSE06 calculations. We used projector-augmented wave (PAW)[35,38] potentials with Zn(3d, 4s), O(2s, 2p), and H(1s) valence states and relaxed structures until forces converged below 10^{-3} eV Å^{-1}. For the hexagonal unit cell, an 8 × 8 × 5 gamma-centered reciprocal space mesh was used, which resulted in PBE lattice parameters a = 3.286 Å, c = 5.307 Å, slightly overestimating the experimental lattice parameters by 1–2% as is common for PBE. For defect calculations, we used a 3 × 3 × 2 supercell (fixed lattice parameters a = 9.859 Å, c = 10.614 Å) for which a 2 × 2 × 2 gamma-centered k-mesh was used.

In this supercell, H_O, H_{Zn}, OH_O, V_O, Zn_i, defects, and H_{Zn}–OH_O, and Zn_i–OH_O defect clusters were computed in various charge states. We computed their formation energy[39,40] as

$$E^q_{form} = E_{def} - E_{perf} - \sum_i n_i\mu_i + q(E_{Fermi} + E_{VBM}) + \Delta E_{corr}, \quad (2)$$

where E_{def} and E_{perf} are the DFT total energies of the defective and stoichiometric cell, respectively, and n_i designates the number of added ($n_i > 0$) or removed ($n_i < 0$) atoms of species i at a chemical potential μ_i. The range of chemical potentials over which ZnO is stable was computed using Pymatgen,[41] considering the competing phases Zn and $ZnOH_2$ as well as molecular O_2, H_2O, and H_2. To account for different charge states, q electrons are exchanged with a reservoir at E_{Fermi}, measured relative to the valence band edge E_{VBM}. The corrective term ΔE_{corr} accounts for the alignment of neutral and charged cells and image-charge effects.[42] Based on these formation energies, we used py-sc-Fermi to compute the self-consistent Fermi energy and the various defect concentrations.[43]

3. Results and discussion

3.1. Structure and morphology of the ZnO nanoparticle powders

Morphological and structural characterization of the ZnO nanoparticles was carried out using transmission electron microscopy (TEM) (Fig. 1). Complementary data from X-ray diffraction (XRD), nitrogen sorption analysis, and thermogravimetric analysis (TGA) are provided in the SI (Fig. S2–S4).

Transmission electron micrographs (Fig. 1) reveal that the as-synthesized nanoparticle powders from both CVS and FSP (Fig. 1a and e) are made up of grains with an equiaxed morphology. Upon thermal annealing to 673 K or 873 K (VA673, VA873 samples, respectively), the particles maintain their initial shape but grow because of ion diffusion-controlled mass transport. This particle growth becomes more pronounced with increasing annealing temperature. The particle size distributions of both the as-synthesized and VA673-treated CVS and FSP samples remain narrow, with median particle sizes of 9 nm (as-synthesized) and 15 nm (VA673) for the CVS materials, and 12 nm (as-synthesized) and 13 nm (VA673) for the FSP materials, respectively (Fig. 1d and h). Annealing at 873 K induces substantial grain coarsening with final median particle sizes of 103 nm and 41 nm for CVS and FSP materials, respectively (Fig. 1d and h). We note that neither type of particle powder shows necking, implying that

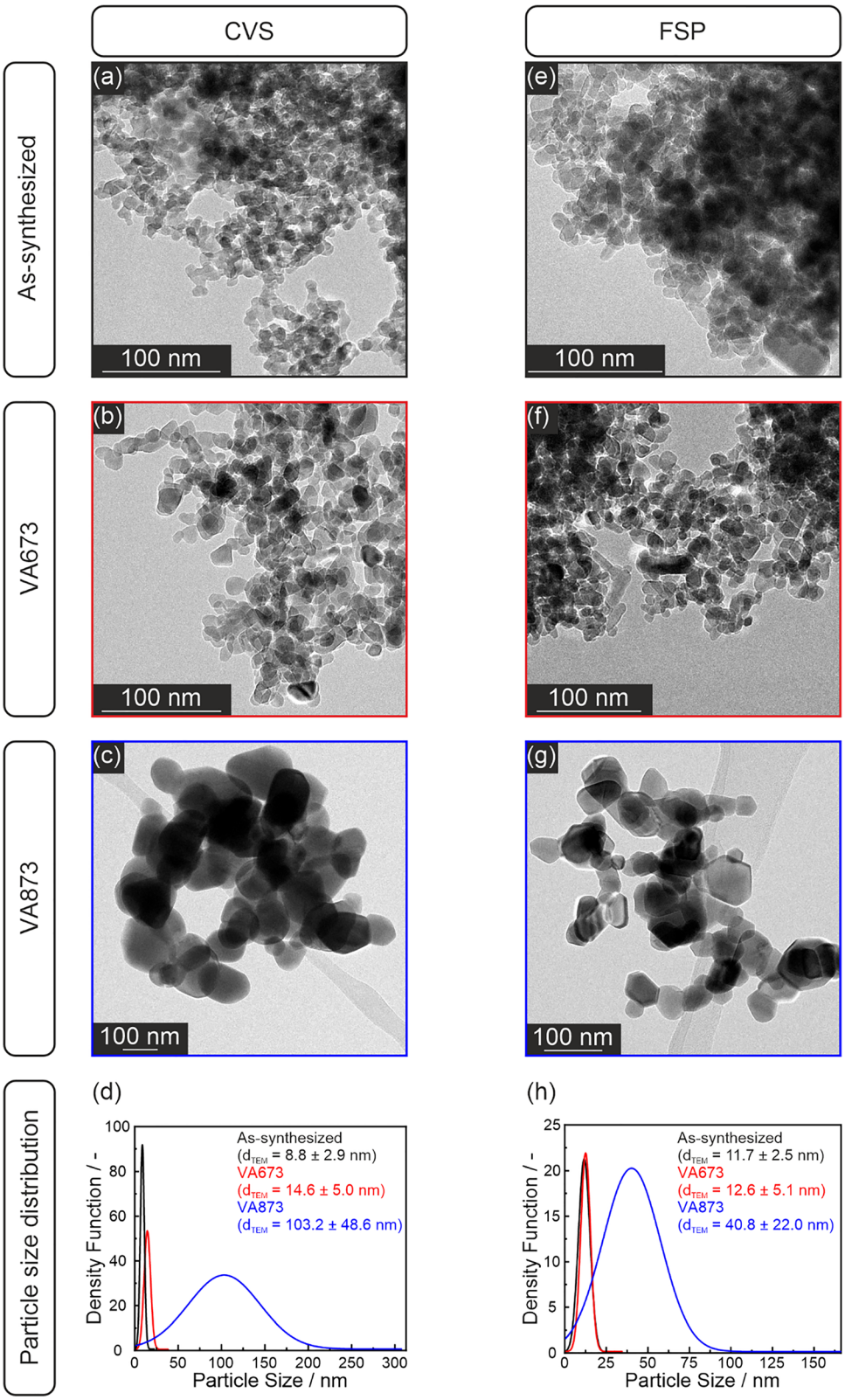

Fig. 1 Transmission electron micrographs of as-synthesized (a) and (e) and thermally annealed ZnO nanoparticle powders – VA673 (b) and (f) and VA873 (c) and (g) – prepared *via* chemical vapor synthesis (CVS, left column) and flame spray pyrolysis (FSP, right column). Corresponding particle size distribution plots are provided in (d) and (h) for CVS- and FSP-derived materials, respectively.

interparticle charge-transport is the same, different behavior thus being ascribed to particle size and surface composition.

3.2. Paramagnetic defects in ZnO nanoparticle powders: a combined experimental and theoretical analysis

To investigate the defect chemistry of the ZnO nanoparticle powders, EPR spectroscopy measurements were performed. Fig. 2 presents the EPR spectra of ZnO nanoparticle powders annealed at 673 K (Fig. 2a and c) and 873 K (Fig. 2b and d). The particle powders were either synthesized *via* CVS (left column) or FSP (right column).

The EPR spectrum of the CVS sample annealed at 673 K (Fig. 2a) exhibits two paramagnetic signals with *g*-values of 2.003 and 1.96. Weaker signals at g = 1.999 and g = 1.982 (indicated by asterisks in Fig. 2a) are attributed to paramagnetic surface impurities that have not yet been fully identified.

The isotropic EPR signal at g = 2.003 is linked to paramagnetic carbonaceous species, such as coke-like residues that form upon pyrolysis of the precursors of the gas phase synthesis and subsequent thermal annealing at 673 K.[19,44,45] Apparently, such species can only be fully removed by oxygen treatment at 873 K[44] (Fig. S4). The *g*-value of 2.003 exceeds that of the free electron spin value (g = 2.0023). This is characteristic of carbon radicals with substantial sp^3 character. Unpaired electrons in dangling bonds of carbon radicals represent a feature that is often observed on metal oxide nanoparticles synthesized *via* metal–organic chemical vapor synthesis (MO-CVS).[44,45] (In contrast, carbon-related radicals with *g*-values below g = 2.0023 are generally associated with electron-containing orbitals of predominantly sp^2 character.[44]) Earlier Auger electron spectroscopy measurements by Gheisi *et al.* were performed on identical materials (ZnO-CVS-VA673) and quantified the surface carbon content at approximately 5 at%.[29] Additionally, FT-IR spectroscopy revealed surface carbonates and carboxylates on the annealed ZnO.[44,46]

The spectra of the CVS-VA873 and the two FSP samples (VA673 and VA873; Fig. 2b–d) exhibit only one paramagnetic signal at g = 1.96 that corresponds to shallow donor states, that

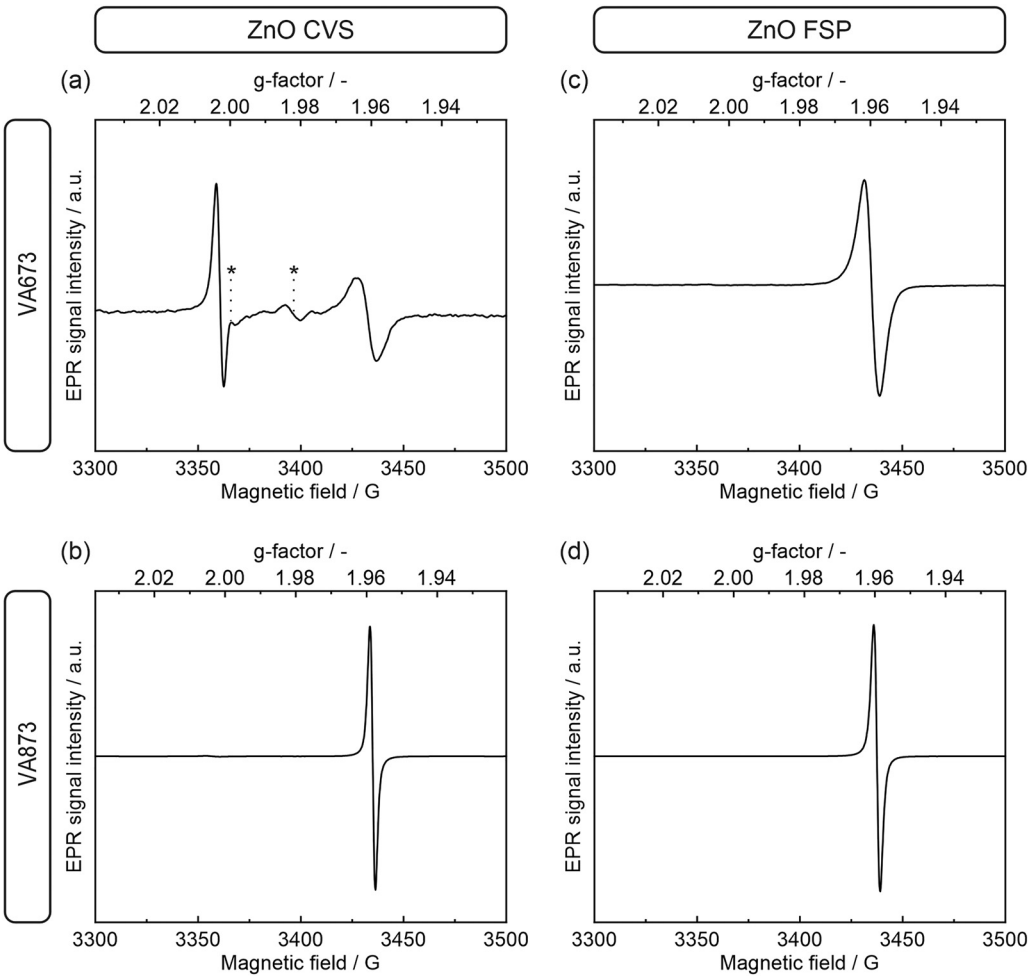

Fig. 2 Electron paramagnetic resonance (EPR) spectra of ZnO nanoparticle powders obtained from (a) CVS-VA673, (b) CVS-VA873, (c) FSP-VA673, and (d) FSP-VA873, recorded at 100 K under continuous pumping ($p < 10^{-5}$ mbar) with a microwave power of 1 mW. Spectra (a–d) are plotted with individual *y*-axis scales to highlight spectral features. For comparison, the intensities of spectra (b)–(d) are scaled relative to (a) by a factor of 6, 4, and 20, respectively.

were previously associated with intrinsic point defects like oxygen vacancies,[20,21,27] zinc interstitials,[19,20,23,27] or extrinsic impurities such as hydrogen[20,22,27] within the ZnO lattice.

The spin concentrations associated with the signal at g = 1.96 are summarized in Table 1, along with the corresponding defect concentrations, Q-factors and peak-to-peak linewidths.

The signals related to the ZnO CVS and FSP samples annealed at temperatures not higher than 873 K exhibit narrower peak-to-peak EPR linewidths compared to those measured for the samples annealed at 673 K (Table 1). Generally, broader EPR signals originate from stronger spin–spin interactions inside systems of higher concentrations (*i.e.*, less dilute spins). These interactions also lead to lower Q-factors measured for the critically coupled cavity. Although samples annealed at 873 K have higher spin concentrations than those treated at 673 K (Table 1), the associated signals exhibit narrower peak-to-peak linewidths. This is explained by powder annealing at 873 K, which not only promotes substantial particle growth (Fig. 1), but it also enables reorganization of the ZnO particle lattice that was formed under non-equilibrium conditions in the gas phase. This enhances the crystallinity of the nanoparticles and eliminates local strain. As a result, and in comparison to the small particles with a more disordered crystal structure and greater lattice strain, internal magnetic field inhomogeneities are reduced, which explains the narrower EPR linewidths in the larger particles.

O_2 gas ($p(O_2)$ = 100 mbar) was introduced into the ZnO nanoparticle powder samples at 100 K to identify potential microwave power-induced saturation effects or quenching effects on the EPR signals induced by spin center interactions with paramagnetic O_2 molecules. The EPR spectra in Fig. 3 represent a comparison between measurements recorded in 100 mbar O_2 atmosphere (blue lines) and measurements recorded in high vacuum ($p < 10^{-5}$ mbar, black lines), both prior to and after O_2 exposure.

In oxygen atmosphere (bottom spectra in blue), the intensity of the signal at g = 2.003 (Fig. 3a) increases significantly, while the signal at g = 1.96 shows constant intensities for all samples (Fig. 3a–d). This intensity enhancement of the signal at g = 2.003 is fully reversible with respect to O_2 pressure. Re-establishing high vacuum conditions ($p < 10^{-5}$ mbar, top spectra in black) restores the original signal intensity value.

The transition related to the g = 2.003 signal shows saturation effects (Fig. 4), as characterized by a leveling off and subsequent decrease in the signal intensity above a microwave power of 0.02 mW. To further analyze this, microwave power-dependent EPR measurements were conducted both under dynamic high vacuum (Fig. 4a) and in an oxygen atmosphere (Fig. 4b).

Measured intensity curves reveal saturation of the transition above microwave power values of 0.02 mW or 0.2 mW in a dynamic vacuum ($p < 10^{-5}$ mbar) and in an O_2 atmosphere, respectively. In an O_2 atmosphere, enhanced spin-lattice relaxation and reduced relaxation times of the spin center explain the onset shift of the saturation regime. Surface adsorbed O_2 enables spin relaxation *via* spin exchange interactions and dipolar coupling. As a result, saturation effects occur at lower microwave powers in the absence of O_2. Consequently, the significant intensity enhancement effect described in Fig. 3a is attributed to surface adsorbed O_2 molecules. Its pressure dependence and reversibility in combination with the g-factor of 2.003 provide clear evidence that the underlying paramagnetic sites – presumably polyaromatic carbon radicals – are located at the grain surfaces, where they can readily interact with O_2.

Conversely, both the signal intensity and peak-to-peak linewidth of the signal at g = 1.96 are not affected by O_2 (Fig. 3), indicating that the corresponding defect must be located in the nanoparticle bulk, where it is not accessible to O_2 gas.

As mentioned above, there exists a variety of hypotheses regarding the nature and origin of the defect related to the g = 1.96 signal.[19–24,27] We conducted density functional theory (DFT) calculations to consistently reevaluate the formation energies of the most likely defects, their charge states and magnetic properties. Gas-phase synthesis involves formation temperatures around 1000 K, particle nucleation and growth in oxygen-deficient and – with hydrocarbons in the precursor solution – hydrogen-rich atmospheres. To mimic these conditions, we set the oxygen and zinc chemical potentials to the zinc-rich and oxygen-poor limit ($\mu_O = \mu_O^0 - 3.27$ eV, $\mu_{Zn} = \mu_{Zn}^0$, the two being linked by $E_{ZnO} = \mu_{Zn} + \mu_O$) and rather hydrogen-rich conditions ($\mu_H = \mu_H^0 - 0.08$ eV, mimicking an approximately 40% hydrogen atmosphere) and assume a temperature of 1000 K. The self-consistent Fermi energy (SC-Fermi) under these conditions is 3.85 eV, with Table 2 providing an overview of the computed defect formation energies and defect concentrations at that Fermi energy.

The two defect candidates with the highest relative abundances are oxygen vacancies (V_O) and hydroxyl groups substituting oxygen lattice sites (OH_O). Both defects exhibit comparably low formation energies of 1.32 and 1.34 eV, respectively, with relative

Table 1 Calculated spin concentrations (signal at g = 1.96), the corresponding concentrations of a related point defect in atomic percent (at%, assuming one spin corresponds to one defect site), Q-factors, and peak-to-peak linewidths for ZnO nanoparticle powders after annealing at 673 K (VA673) or 873 K (VA873), as determined from spectra in Fig. 2

Sample	Spin concentration (g = 1.96) [spins cm^{-3} ($\times 10^{17}$)]	Defect concentration [at% ($\times 10^{-4}$)]	Q-factor	Peak-to-peak linewidth ΔB [G]
CVS-VA673	0.25	0.30	9900	9.4
CVS-VA873	1.19	1.44	2900	2.6
FSP-VA673	1.30	1.56	8800	7.4
FSP-VA873	1.92	2.31	8400	3.3

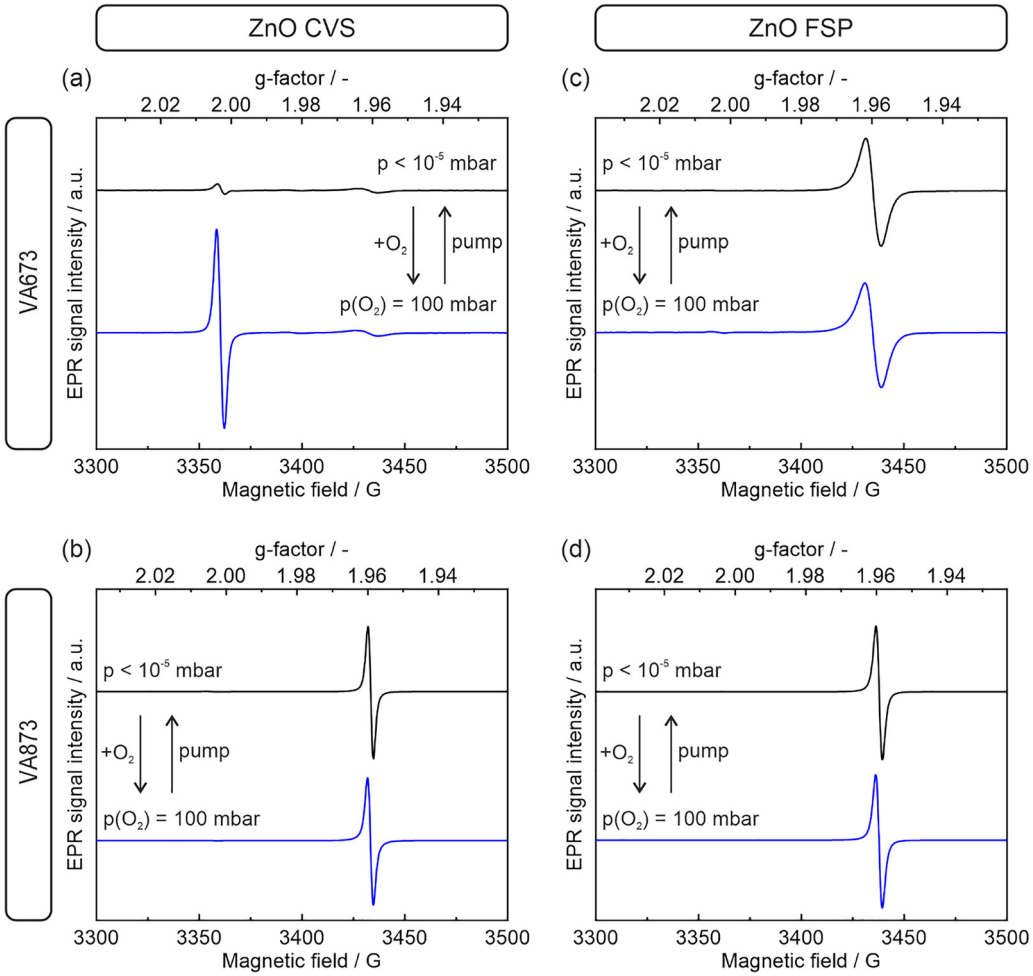

Fig. 3 EPR spectra of ZnO nanoparticle powders obtained from (a) CVS-VA673, (b) CVS-VA873, (c) FSP-VA673, and (d) FSP-VA873, recorded at $p < 10^{-5}$ mbar (top/black spectra) or in an oxygen atmosphere ($p(O_2)$ = 100 mbar, bottom/blue spectra) at 100 K. Spectra (a–d) are plotted with individually adjusted y-axis scales. The y-axis scales for (b)–(d) are reduced by factors of 1.7, 2.5, or increased by a factor of 2 relative to the spectrum (a), respectively.

abundances that are at least two orders of magnitude higher than those of alternative defect candidates (Table 2).

These two defects, including their potential paramagnetic states, are considered for further analysis. Although V_O and OH_O are the most abundant defects, they are not necessarily paramagnetic. An oxygen vacancy in zinc oxide can exist in three charge states: (i) neutral V_O^0, where both electrons remain in the vacancy, (ii) singly charged V_O^+, where one electron is removed from the vacancy, and (iii) doubly charged V_O^{2+}, where both electrons are removed from the vacancy. Only the singly charged oxygen vacancy V_O^+, hosting an unpaired electron, is EPR active. Similarly, a hydroxyl group that substitutes an oxygen lattice site can exist in two charge states: (i) as a neutral OH_O^0 defect, where an O^{2-} ion binds a neutral hydrogen atom (H) to form a hydroxyl group, and (ii) as a positively charged OH_O^+ defect, where the O^{2-} ion carries a H^+ instead. Only the neutral charge state hosts an unpaired electron – the $1s^1$ electron of the hydrogen atom – making it EPR active.

Fig. 5 shows the defect formation energies as a function of the Fermi energy for each charge state of oxygen vacancies (blue lines) and hydroxyl groups substituting oxygen lattice sites (orange lines).

The most probable charge state of a specific defect corresponds to the one with the lowest formation energy under the assumed synthesis conditions. According to Fig. 5, the paramagnetic singly charged oxygen vacancy (V_O^+) never adopts the lowest formation energy across the entire Fermi energy range and therefore never represents the thermodynamically most stable charge state. Furthermore, Fig. 5 shows that for oxygen vacancies (blue lines) the transition level (TL), where both the neutral (V_O^0) and doubly charged (V_O^{2+}) charge states have identical formation energy (E_f = 1.32 eV), is located at a Fermi energy of 2.60 eV. Below 2.60 eV, the V_O^{2+} defect represents the most stable charge state, whereas above 2.60 eV, the V_O^0 defect becomes the most stable charge state (Fig. 5).

For hydroxyl groups substituting oxygen sites in the ZnO lattice (orange lines in Fig. 5), the transition level (TL) between the neutral (OH_O^0) and the singly charged (OH_O^+) states occurs at a Fermi energy of 3.78 eV with a formation energy of 1.34 eV. Below 3.78 eV, the singly charged state (OH_O^+) with the electron in the

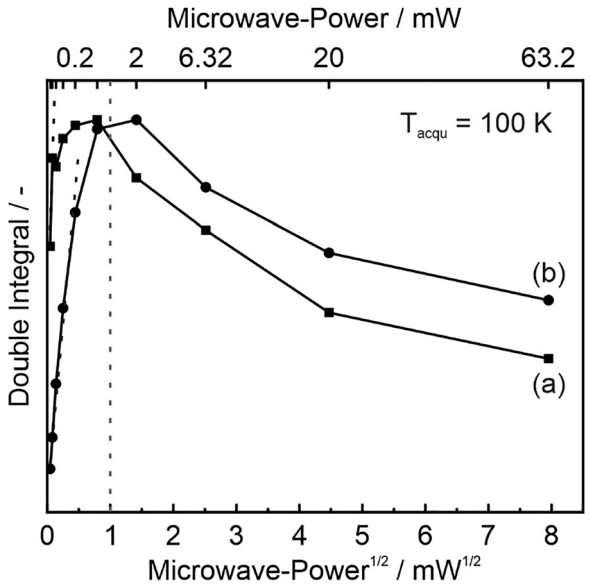

Fig. 4 Microwave power saturation curves of the EPR signal at g = 2.003, recorded at 100 K and (a) at $p < 10^{-5}$ mbar and (b) in oxygen atmosphere ($p(O_2)$ = 100 mbar).

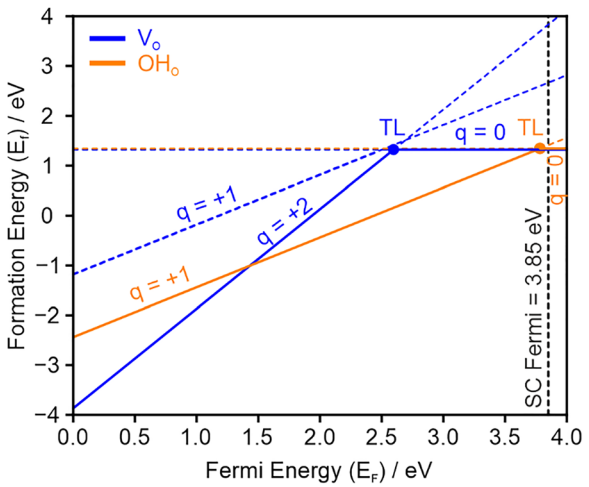

Fig. 5 Defect formation energies plotted as a function of Fermi energy for oxygen vacancies (V_O, blue lines) in three charge states (q = 0, +1, +2), and hydroxyl groups substituting oxygen lattice sites (OH_O, orange lines) in two charge states (q = 0, +1), including their charge transition levels (TLs). Thermodynamically stable charge states are represented by solid lines, while unstable charge states are indicated by dashed lines.

Table 2 Point defect candidates at the origin of the paramagnetic signal at g = 1.96, formation energies of their most stable charge states – calculated at a Fermi energy of 3.85 eV – and their relative abundance

Defect candidate	Formation energy [eV]	Percentage of defective sites [%]
Zn_i	3.95	1.41×10^{-18}
V_O	1.32	2.17×10^{-5}
H_O	1.71	4.70×10^{-7}
OH_O	1.34	2.44×10^{-5}
H_{Zn}	4.37	9.60×10^{-21}
Zn_i–H_O	4.94	2.39×10^{-23}
H_{Zn}–OH_O	3.40	7.75×10^{-16}

Table 3 DFT-derived formation energies of each charge state, corresponding concentrations (C_q), para- or diamagnetism, and relative abundances for oxygen vacancies (V_O) and hydroxyl groups substituting oxygen lattice sites (OH_O)

Defect species	Charge state (q)	Formation energy [eV]	Concentration (C_q) [cm^{-3}]	EPR active	Relative population [%]
V_O	0	1.32	8.75×10^{15}	✗	100
	+1	2.68	1.33×10^{9}	✓	0
	+2	3.84	1.84×10^{3}	✗	0
OH_O	0	1.34	6.85×10^{15}	✓	69.8
	+1	1.42	2.97×10^{15}	✗	30.2

conduction band is more stable, while the paramagnetic neutral state (OH_O^0) becomes energetically preferred above 3.78 eV (Fig. 5).

The concentration (defects per cubic centimeter) C_q of a defect in a charge state q, was determined based on eqn (3), which follows an Arrhenius-type relationship.

$$C_q = N \cdot \exp\left(-\frac{E_f^q}{k_B \cdot T}\right) \quad (3)$$

N: number of available sites per volume where the defect can form E_f^q: defect formation energy of the charge state q, k_B: Boltzmann constant, T: temperature.

Table 3 summarizes the DFT results for oxygen vacancies (V_O) and hydroxyl groups substituting oxygen lattice sites (OH_O). It reports the formation energies of the two defects in each charge state, corresponding concentrations (C_q), its para- or diamagnetism, and finally its relative abundance.

The formation energy of 1.32 eV of the neutral oxygen vacancy (V_O^0) is significantly lower than those of the charged defects, with $E_f(V_O^+)$ = 2.68 eV and $E_f(V_O^{2+})$ = 3.84 eV (Table 3). Consequently, the concentration of the diamagnetic V_O^0 is at least six orders of magnitude higher than that of the charged states (V_O^+, V_O^{2+}, Table 3).

On the other hand, the formation energies of both the neutral (OH_O^0) and singly positively charged (OH_O^+) states, with values of 1.34 eV and 1.42 eV, respectively, are relatively close (Table 3). Consequently, their concentrations are similar (Table 3), and both charge states exist with relative abundances of 69.8% for the paramagnetic OH_O^0 state and 30.2% for the diamagnetic OH_O^+ state (Table 3).

Thus, under the given experimental conditions, defects of the OH_O^0 type are the most likely candidates for explaining the EPR resonance at a g-value of 1.96 in ZnO lattices.

To experimentally support that OH_O^0 defects serve as shallow donor states, ZnO nanoparticle samples were exposed at room temperature to a mixed atomic and molecular hydrogen atmosphere and, in a subsequent experiment, to a purely molecular hydrogen atmosphere ($p(H^\bullet) = p(H_2)$) = 7×10^{-3} mbar) (Fig. 6a).

Atomic hydrogen exposure of the ZnO sample produces a significant intensity increase of the EPR signal at g = 1.96 (Fig. 6a). The calculated numbers of spins (Fig. 6c) reveal a five-fold increase of the spin concentration. (Note that the

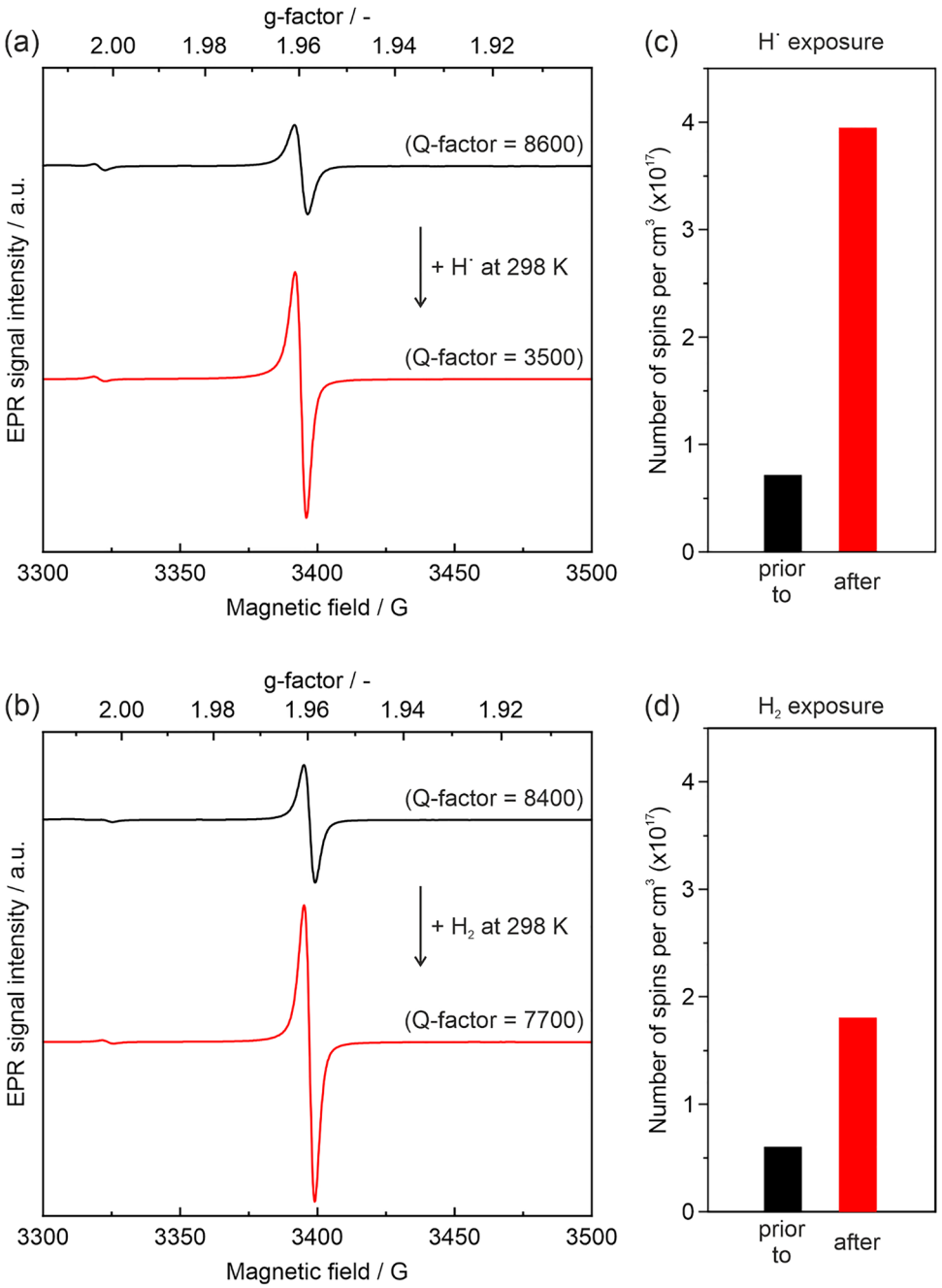

Fig. 6 EPR spectra of a ZnO nanoparticle powder (CVS-VA873) prior to (black lines) and after (red lines) sample exposure to (a) mixed atomic and molecular hydrogen and (b) purely molecular hydrogen for 3 hours at room temperature. Panels (c) and (d) plot the spin concentrations, calculated from the measured signal intensities at 10 K and under static vacuum conditions ($p < 10^{-4}$ mbar), using a microwave power of 1 mW for EPR spectrum acquisition.

number of spins cannot be determined from direct comparison of the EPR signal intensities alone; the Q-factor measured for the critically coupled cavity and related to each measurement (Fig. 6), impacts the EPR signal intensity as well (eqn (1)).

The observed increase in spin concentration corresponds to additionally formed paramagnetic species of an identical defect. Respective microwave power-dependent EPR measurements (Fig. S5) rule out saturation effects as the potential source for this effect.

Thus, the experiment supports the conclusions drawn from DFT simulations, that OH_O^0 defects are the primary contributors to the EPR resonance at $g = 1.96$. The following reaction pathway which outlines the hydrogenation of the lattice is proposed:

$$O_O + H^\bullet \rightarrow OH_O^0 \quad (4)$$

A follow-up experiment was performed with molecular hydrogen ($p(H_2) = 7 \times 10^{-3}$ mbar, 3 h; Fig. 6b) to determine

whether H_2 dissociation at the ZnO nanoparticle surfaces[47–49] can induce such a reaction pathway for defect formation or not. Again a significant increase in the EPR signal intensity at g = 1.96 was observed (Fig. 6b): the corresponding number of spins increased by a factor of three (Fig. 6d and Fig. S6).

Hydrogen dissociation at ZnO particle surfaces has been reported in the literature.[47–49] It can occur either (i) homolytically, where each hydrogen atom forms a hydrogen radical ($H^\bullet$), and/or (ii) heterolytically, where hydride groups H^- and protons H^+ form at surface Zn^{2+}–O^{2-} sites, respectively. In a subsequent step hydride oxidation (eqn (5)) gives rise to $H^\bullet$ radicals, and – as concluded from the result described along Fig. 6b – produces additional shallow donor states (eqn (4)):

$$H^- \rightarrow H^\bullet + e^- \quad (5)$$

Atomic hydrogen ($H^\bullet$) can directly diffuse into the lattice of ZnO nanoparticles, where it forms OH_O defects, whereas molecular hydrogen (H_2) must first dissociate to form $H^\bullet$ radicals. This would explain that sample contact with atomic hydrogen produces approximately twice as many additional paramagnetic defects as molecular hydrogen, with enhancement factors of 5.5 and 3, respectively (Fig. 6).

Enhanced spin concentrations related to the signal at g = 1.96, resulting from ZnO particle exposure to atomic and molecular hydrogen (Fig. 6), strongly support the argument derived from DFT calculations that the shallow donor states – observed in ZnO samples from very different synthesis approaches[22,50,51] – correspond to OH_O^0 formed at oxygen lattice sites (Tables 2 and 3).

These findings represent an important and significant complement to earlier reports in the literature, which consistently identify hydrogen as a ubiquitous impurity in ZnO, independent of the growth method.[50] Its incorporation is facilitated by the low formation energy of interstitial H^+, leading to substantial hydrogen concentrations even in nominally undoped samples.[50,52] This behavior contrasts with that in most other semiconductors, where hydrogen typically acts as a compensating impurity.[22,52] In ZnO, however, hydrogen contributes significantly to the intrinsic n-type conductivity.[22,53,54] Thomas *et al.*[54] demonstrated that hydrogen diffusion into the ZnO lattice enhances its conductivity and proposed two possible impurity configurations: interstitial protons migrating between lattice sites, and complexes formed between protons and oxygen anions. This interpretation is supported by DFT calculations by Van de Walle, who identified interstitial hydrogen as a shallow donor defect, thereby providing a theoretical framework for its conductivity-enhancing role.[52] Spectroscopic investigations by Lavrov *et al.*[55] and Herklotz *et al.*[56] employing Raman, infrared (IR), and photoluminescence (PL) techniques, revealed two predominant hydrogen-related shallow donor configurations: hydrogen located at the bond-centered lattice site (H_{BC}) and hydrogen bound to oxygen vacancies (H_O), with H_{BC} being the more prominent contributor. Complementarily, electron paramagnetic resonance (EPR) studies by Lee *et al.*[51] and Hofmann *et al.*[22] reported paramagnetic signals near a g-value of 1.957 in nominally undoped ZnO, which were attributed to shallow donor states.

These reports support the assignment of the paramagnetic defect resonating at g = 1.96 to paramagnetic OH_O^0 centers, which originate from the hydrogenation of the ZnO lattice. In this configuration, the unpaired 1s electron of the hydrogen atom gives rise to the observed EPR signal. In principle, this should lead to hyperfine splitting of the EPR signal into two distinct lines due to interactions between the unpaired electrons and the hydrogen nuclei.

Our measurements, however, reveal only a single EPR line (Fig. 6) that is exempt from any resolvable hyperfine structure. This discrepancy is attributed to the relatively broad linewidth of the observed EPR signal, which likely obscures the expected splitting. For comparison, Hofmann *et al.*[22] employed electron nuclear double resonance (ENDOR) spectroscopy to resolve hyperfine interactions of shallow hydrogen donors in ZnO, reporting a hyperfine constant of 1.4 MHz, corresponding to approximately 0.5 Gauss. With linewidths of 2.6 to 9.4 Gauss (Table 1) the signals from the here reported EPR spectra exceed this value, rendering the hyperfine doublet unresolvable (Fig. 6).

The concentration of paramagnetic shallow trap states, which are determined using EPR signal intensity measurements and known sample weights, allow making very important conclusions about the apparently unavoidable minimum doping of ZnO nanocrystals with hydrogen. The corresponding defect concentrations, which are in the range of 10^{17} cm^{-3} (10^{-4} at%), are the lower limit of impurities, because they correspond only to a fraction of the paramagnetic centers. The increase in intensity of the EPR signals through annealing in a hydrogen-free atmosphere and at 873 K clearly shows that there is a pool of diamagnetic hydrogen in the crystallites, a fraction of which then becomes OH_O^0 centers.

Even as a trace element, hydrogen has a significant influence on the optoelectronic properties of ZnO in the form of single crystals, thin films, or in form of nano- and microparticulate functional materials. This work and in particular the robust assignment of the EPR resonance at g = 1.96 to the OH_O^0 defect and, thus, to the hydrogenation of the ZnO lattice, lays a material chemistry foundation for defect engineering and future correlations between synthesis, adjustment of the solid's hydrogen content, and its functional properties.

4. Conclusions

This study investigated the origin and formation mechanisms of the paramagnetic EPR signal at g = 1.96 in gas-phase synthesized ZnO nanoparticle samples. Based on DFT calculations and further corroborated by hydrogen exposure experiments, this defect was attributed to neutral hydroxylated oxygen sites (OH_O^0), formed through hydrogenation of the ZnO lattice. The significant abundance of such hydrogen-related defects indicates that hydrogen is unintentionally incorporated during synthesis. The increase in defect concentration

upon exposure to both atomic and molecular hydrogen underlines the capacity of the ZnO lattice to incorporate hydrogen. The observed increase that follows sample exposure to molecular H_2 indicates that H_2-dissociation takes place at the ZnO grain surfaces to further initiate lattice protonation. These findings provide new insights into the defect chemistry of ZnO nanoparticles, emphasizing the role of hydrogen in defect formation as well as the high probability for hydrogen incorporation during nanoparticle synthesis at high temperatures, even in the absence of hydrogen-containing solvents. This understanding is crucial for tailoring ZnO properties for applications in sensing, catalysis, and electronic applications, by modulation of the electronic conductivity and gas adsorption strength.

Author contributions

Korbinian Aicher: investigation, formal analysis, data curation, writing – original draft; Thomas Berger: formal analysis, data curation, writing, review & editing; Ulrich Aschauer, formal analysis, review and editing; Oliver Diwald: supervision, funding acquisition, conceptualization, writing – original draft, review & editing.

Conflicts of interest

There are no conflicts to declare.

Data availability

Data for this article, including computational, structural and spectroscopic data are available at MATERIALSCLOUD at **https://doi.org/10.24435/materialscloud:f8-mc**.

The data supporting this article have been included as part of the supplementary information (SI). Supplementary information: additional structural and morphological information was obtained through X-ray diffraction (XRD), nitrogen sorption analysis (BET), and thermogravimetric analysis (TGA). Furthermore, saturation curves of ZnO-CVS-VA873 nanoparticles prior to and after exposure to atomic and molecular hydrogen are presented. See DOI: **https://doi.org/10.1039/d5tc03036f**.

Acknowledgements

This research was funded in whole by the Austrian Science Fund (FWF) [10.55776/P 34906]. Calculations were performed using supercomputer resources provided by the Vienna Scientific Cluster (VSC). For open access purposes, the author has applied a CC BY public copyright license to any author accepted manuscript version arising from this submission.

References

1 O. Diwald, In Zinc Oxide Nanoparticles for Varistors, *Metal Oxide Nanoparticles*, ed O. Diwald, T. Berger, Wiley, 2021, pp. 783–807.
2 S. C. Pillai, J. M. Kelly, R. Ramesh and D. E. McCormack, Advances in the synthesis of ZnO nanomaterials for varistor devices, *J. Mater. Chem. C*, 2013, **1**, 3268.
3 T. J. Boyle, S. D. Bunge, N. L. Andrews, L. E. Matzen, K. Sieg, M. A. Rodriguez and T. J. Headley, Precursor Structural Influences on the Final ZnO Nanoparticle Morphology from a Novel Family of Structurally Characterized Zinc Alkoxy Alkyl Precursors, *Chem. Mater.*, 2004, **16**, 3279–3288.
4 C. Baratto, G. Sberveglieri, A. Onischuk, B. Caruso and S. Di Stasio, Low temperature selective NO2 sensors by nanostructured fibres of ZnO, *Sens. Actuators, B*, 2004, **100**, 261–265.
5 H.-M. Lin, S.-J. Tzeng, P.-J. Hsiau and W.-L. Tsai, Electrode effects on gas sensing properties of nanocrystalline zinc oxide, *Nanostruct. Mater.*, 1998, **10**, 465–477.
6 T. Berger, Metal Oxide Nanoparticle-Based Conductometric Gas Sensors. *In Metal Oxide Nanoparticles*, ed O. Diwald, T. Berger, Wiley, 2021, pp. 809–834.
7 X. Wang, F. Sun, Y. Duan, Z. Yin, W. Luo, Y. Huang and J. Chen, Highly sensitive, temperature-dependent gas sensor based on hierarchical ZnO nanorod arrays, *J. Mater. Chem. C*, 2015, **3**, 11397–11405.
8 T.-H. Hsieh, J.-Y. Chen, C.-W. Huang and W.-W. Wu, Observing Growth of Nanostructured ZnO in Liquid, *Chem. Mater.*, 2016, **28**, 4507–4511.
9 S. Y. Cho, Y. H. Kang, J.-Y. Jung, S. Y. Nam, J. Lim, S. C. Yoon, D. H. Choi and C. Lee, Novel Zinc Oxide Inks with Zinc Oxide Nanoparticles for Low-Temperature, Solution-Processed Thin-Film Transistors, *Chem. Mater.*, 2012, **24**, 3517–3524.
10 Y.-J. Chiang and C.-C. Lin, Photocatalytic decolorization of methylene blue in aqueous solutions using coupled ZnO/SnO_2 photocatalysts, *Powder Technol.*, 2013, **246**, 137–143.
11 S. H. Li and Z. F. Liu, Enhanced photocatalytic activity of core shell SnO2/ZnO photocatalysts, *Mater. Technol.*, 2013, **28**, 234–237.
12 P. Zhu, Y. Chen, M. Duan, M. Liu, P. Zou and M. Zhou, Enhanced visible photocatalytic activity of Fe-Cu-ZnO/graphene oxide photocatalysts for the degradation of organic dyes, *Can. J. Chem. Eng.*, 2018, **96**, 1479–1488.
13 J. N. Schrauben, R. Hayoun, C. N. Valdez, M. Braten, L. Fridley and J. M. Mayer, Titanium and Zinc Oxide Nanoparticles Are Proton-Coupled Electron Transfer Agents, *Science*, 2012, **336**, 1298–1301.
14 W. Zhang, R. Zhu, X. Liu, B. Liu and S. Ramakrishna, Facile construction of nanofibrous ZnO photoelectrode for dye-sensitized solar cell applications, *Appl. Phys. Lett.*, 2009, 95.
15 S. I. Al-Saeedi, Photoelectrochemical Green Hydrogen Production Utilizing ZnO Nanostructured Photoelectrodes, *Micromachines*, 2023, 14.
16 K. Aicher, T. Berger, U. Aschauer and O. Diwald, Activation and Cold Sintering of commercial ZnO Powders: Compaction-induced oxide reduction, *J. Eur. Ceram. Soc.*, 2026, **46**(2), DOI: **10.1016/j.jeurceramsoc.2025.117769**.
17 A. Lauria and M. Niederberger, Controlled Impurity Admixture: From Doped Systems to Composites. *In Metal Oxide Nanoparticles*, ed O. Diwald, T. Berger, Wiley, 2021, pp. 151–183.

18 M. Niedermaier, T. Schwab and O. Diwald, Nanoparticle Synthesis in the Gas Phase, *In Metal Oxide Nanoparticles*, ed. O. Diwald, T. Berger, Wiley, 2021, pp. 67–108.
19 M. Kakazey, M. Vlasova, E. A. Juarez-Arellano, T. Torchynska and V. A. Basiuk, Defect states and morphological evolution in mechanically processed ZnO + xC nanosystems as studied by EPR and photoluminescence spectroscopy, *RSC Adv.*, 2016, **6**, 58709–58722.
20 D. Savchenko, A. Vasin, O. Kuz, I. Verovsky, A. Prokhorov, A. Nazarov, J. Lančok and E. Kalabukhova, Role of the paramagnetic donor-like defects in the high n-type conductivity of the hydrogenated ZnO microparticles, *Sci. Rep.*, 2020, **10**, 17347.
21 A. Janotti and C. G. van de Walle, Native point defects in ZnO, *Phys. Rev. B: Condens. Matter Mater. Phys.*, 2007, 76.
22 D. M. Hofmann, A. Hofstaetter, F. Leiter, H. Zhou, F. Henecker, B. K. Meyer, S. B. Orlinskii, J. Schmidt and P. G. Baranov, Hydrogen: a relevant shallow donor in zinc oxide, *Phys. Rev. Lett.*, 2002, **88**, 45504.
23 L. S. Vlasenko and G. D. Watkins, Optical detection of electron paramagnetic resonance for intrinsic defects produced in ZnO by 2.5-MeV electron irradiation in situ at 4.2 K, *Phys. Rev. B: Condens. Matter Mater. Phys.*, 2005, 72.
24 J. J. Schneider, R. C. Hoffmann, J. Engstler, A. Klyszcz, E. Erdem, P. Jakes, R.-A. Eichel, L. Pitta-Bauermann and J. Bill, Synthesis, Characterization, Defect Chemistry, and FET Properties of Microwave-Derived Nanoscaled Zinc Oxide, *Chem. Mater.*, 2010, **22**, 2203–2212.
25 V. Ischenko, S. Polarz, D. Grote, V. Stavarache, K. Fink and M. Driess, Zinc Oxide Nanoparticles with Defects, *Adv. Funct. Mater.*, 2005, **15**, 1945–1954.
26 A. B. Djurišić and Y. H. Leung, Optical properties of ZnO nanostructures, *Small*, 2006, **2**, 944–961.
27 J. E. Stehr, B. K. Meyer and D. M. Hofmann, Magnetic Resonance of Impurities, Intrinsic Defects and Dopants in ZnO, *Appl. Magn. Reson.*, 2010, **39**, 137–150.
28 M. J. Elser, E. Neige, T. Berger, M. Chiesa, E. Giamello, K. McKenna, T. Risse and O. Diwald, On the Importance of Nanoparticle Necks and Carbon Impurities for Charge Trapping in TiO_2, *J. Phys. Chem. C*, 2023, **127**, 8778–8787.
29 A. R. Gheisi, C. Neygandhi, A. K. Sternig, E. Carrasco, H. Marbach, D. Thomele and O. Diwald, O2 adsorption dependent photoluminescence emission from metal oxide nanoparticles, *Phys. Chem. Chem. Phys.*, 2014, **16**, 23922–23929.
30 T. Schwab, M. Niedermaier, K. Aicher, M. S. Elsässer, G. A. Zickler and O. Diwald, Always cubes: A comparative evaluation of gas phase synthesis methods and precursor selection for the production of MgO nanoparticles, *Open Ceram.*, 2021, **6**, 100104.
31 T. Schwab, K. Aicher, H. Razouq, G. A. Zickler and O. Diwald, Segregation Engineering in MgO Nanoparticle-Derived Ceramics: The Impact of Calcium and Barium Admixtures on the Microstructure and Light Emission Properties, *ACS Appl. Mater. Interfaces*, 2021, **13**, 25493–25502.
32 J. M. Jiménez, G. A. Zickler, G. J. Redhammer and T. Berger, Chemical reduction of porous WO3 and TiO2 photoelectrocatalysts by atomic hydrogen, *Appl. Catal., A*, 2023, **658**, 119163.
33 G. Kresse and J. Hafner, Ab initio molecular-dynamics simulation of the liquid-metal-amorphous-semiconductor transition in germanium, *Phys. Rev. B: Condens. Matter Mater. Phys.*, 1994, **49**, 14251–14269.
34 G. Kresse and J. Furthmüller, Efficiency of ab-initio total energy calculations for metals and semiconductors using a plane-wave basis set, *Comput. Mater. Sci.*, 1996, **6**, 15–50.
35 G. Kresse and D. Joubert, From ultrasoft pseudopotentials to the projector augmented-wave method, *Phys. Rev. B: Condens. Matter Mater. Phys.*, 1999, **59**, 1758–1775.
36 J. P. Perdew, K. Burke and M. Ernzerhof, Generalized Gradient Approximation Made Simple, *Phys. Rev. Lett.*, 1996, **77**, 3865–3868.
37 A. V. Krukau, O. A. Vydrov, A. F. Izmaylov and G. E. Scuseria, Influence of the exchange screening parameter on the performance of screened hybrid functionals, *J. Chem. Phys.*, 2006, **125**, 224106.
38 P. E. Blöchl, Projector augmented-wave method, *Phys. Rev. B: Condens. Matter Mater. Phys.*, 1994, **50**, 17953–17979.
39 S. B. Zhang and J. E. Northrup, Chemical potential dependence of defect formation energies in GaAs: Application to Ga self-diffusion, *Phys. Rev. Lett.*, 1991, **67**, 2339–2342.
40 C. Freysoldt, B. Grabowski, T. Hickel, J. Neugebauer, G. Kresse, A. Janotti and C. G. van de Walle, First-principles calculations for point defects in solids, *Rev. Mod. Phys.*, 2014, **86**, 253–305.
41 S. P. Ong, W. D. Richards, A. Jain, G. Hautier, M. Kocher, S. Cholia, D. Gunter, V. L. Chevrier, K. A. Persson and G. Ceder, Python Materials Genomics (pymatgen): A robust, open-source python library for materials analysis, *Comput. Mater. Sci.*, 2013, **68**, 314–319.
42 S. Lany and A. Zunger, Accurate prediction of defect properties in density functional supercell calculations, *Modelling Simul. Mater. Sci. Eng.*, 2009, **17**, 84002.
43 GitHub, GitHub – bjmorgan/py-sc-Fermi: py-sc-Fermi is a materials modelling code for calculating self-consistent Fermi energies and defect concentrations under thermodynamic equilibrium (or quasi-equilibrium) given defect formation energies, 2025, **https://github.com/bjmorgan/py-sc-fermi**, Accessed 16 July 2025.
44 K. Kocsis, M. Niedermaier, T. Schwab, V. Kasparek, T. Berger and O. Diwald, Exciton Emission and Light-Induced Charge Separation in Colloidal ZnO Nanocrystals, *ChemPhotoChem*, 2018, **2**, 994–1001.
45 R. I. Samoilova, A. V. Astashkin, V. V. Kurshev, S. Y. Burilyn, I. I. Frolova and L. N. Rachkovskaya, EPR and ENDOR study of carbon-mineral sorbents, *Appl. Magn. Reson.*, 1994, **7**, 469–477.
46 K. Kocsis, M. Niedermaier, J. Bernardi, T. Berger and O. Diwald, Changing interfaces: Photoluminescent ZnO nanoparticle powders in different aqueous environments, *Surf. Sci.*, 2016, **652**, 253–260.
47 B. Song and L.-H. Xie, H2 Activation Mechanisms on ZnO-Based Catalysts, *J. Phys. Chem. C*, 2025, **129**, 4825–4840.

48 B. S. Mun, Z. Liu, M. A. Motin, P. C. Roy and C. M. Kim, In situ observation of H2 dissociation on the ZnO (0001) surface under high pressure of hydrogen using ambient-pressure XPS, *Int. J. Hydrogen Energy*, 2018, **43**, 8655–8661.
49 H. Noei, H. Qiu, Y. Wang, M. Muhler and C. Wöll, Hydrogen loading of oxide powder particles: A transmission IR study for the case of zinc oxide, *ChemPhysChem*, 2010, **11**, 3604–3607.
50 N. T. Son, J. Isoya, I. G. Ivanov, T. Ohshima and E. Janzén, Hydrogen at zinc vacancy of ZnO: An EPR and ESEEM study, *AIP Conf. Proc.*, 2014, **1583**, 341–344.
51 Y. H. Lee, K. W. Lee, G. W. Jeon and C. E. Lee, Electron paramagnetic resonance and 1H nuclear magnetic resonance study of Y-doping effect on the hydrogen shallow donors in ZnO nanoparticles, *Curr. Appl. Phys.*, 2019, **19**, 1015–1018.
52 C. G. Van De Walle, Hydrogen as a cause of doping in zinc oxide, *Phys. Rev. Lett.*, 2000, **85**, 1012–1015.
53 E. Mollwo, Die Wirkung von Wasserstoff auf die Leitfähigkeit und Lumineszenz von Zinkoxydkristallen, *Z. Phys.*, 1954, **138**, 478–488.
54 D. G. Thomas and J. J. Lander, Hydrogen as a Donor in Zinc Oxide, *J. Chem. Phys.*, 1956, **25**, 1136–1142.
55 E. V. Lavrov, F. Herklotz and J. Weber, Identification of two hydrogen donors in ZnO, *Phys. Rev. B: Condens. Matter Mater. Phys.*, 2009, 79.
56 F. Herklotz, E. V. Lavrov and J. Weber, Photoluminescence study of hydrogen donors in ZnO, *Phys. B*, 2009, **404**, 4349–4353.